Title
Variability of Moderate-Luminosity Active Galactic Nuclei at z = 0.36

Journal
The Astrophysical Journal, 661(1)

ISSN
0004-637X

Authors
Woo, Jong-Hak
Treu, Tommaso
Malkan, Matthew A
et al.

Publication Date
2007-05-20

DOI
10.1086/516564

Peer reviewed

Preprint typeset using LaTeX style emulateapj v. 08/22/09

VARIABILITY OF MODERATE LUMINOSITY ACTIVE GALACTIC NUCLEI AT Z=0.36

Jong-Hak Woo[1], Tommaso Treu[1], Matthew A. Malkan[2], Matthew A. Ferry[3], Tony Misch[4]

(Accepted Feb. 5 2007)

ABSTRACT

We monitored 13 moderate luminosity active galactic nuclei at z=0.36 to measure flux variability, explore feasibility of reverberation mapping, and determine uncertainties on estimating black hole mass from single-epoch data. Spectra and images were obtained with approximately weekly cadence for up to 4 months, using the KAST spectrograph on the 3-m Shane Telescope. In broad band we detect peak-to-peak variations of 9-37% and rms variations of 2-10%. The observed flux variability in the g' band (rest-frame 2800-4000Å) is consistent with that in the r' band (rest-frame 4000-5200Å), but with larger amplitude. However, after correcting for stellar light dilution, using Hubble Space Telescope images, we find nuclear variability of 3-24% (rms variation) with similar amplitudes in the g' and r' bands within the errors. Intrinsic flux variability of the Hβ line is also detected at the 3-13% level, after accounting for systematic errors on the spectrophotometry. This demonstrates that a reverberation mapping campaign beyond the local universe can be carried out with a 3-m class telescope, provided that sufficiently long light curves are obtained. Finally, we compare the Hβ FWHM measured from mean spectra with that measured from single-epoch data, and find no bias but an rms scatter of 14%, mostly accounted for by the uncertainty on FWHM measurements. The propagated uncertainty on black hole mass estimates, due to the FWHM measurement errors using low S/N (10–15 per pixel) single-epoch spectra, is 30%.

Subject headings: galaxies: active — galaxies: nuclei — quasars: general

1. INTRODUCTION

The mass of supermassive black holes (M_{BH}) is the key parameter in understanding the physics of Active Galactic Nuclei (AGNs) and the role of black holes in galaxy formation and evolution, as indicated in the local universe by the tight relations between M_{BH} and host galaxy properties (Ferrarese & Merritt 2000; Gebhardt et al. 2000; Magorrian et al. 1998; Marconi & Hunt 2003; Haring & Rix 2004). However, direct dynamical measurements of M_{BH} using spatially resolved kinematics of stars and gas around the central black hole are limited to the local universe, where only about three dozen masses have been measured (see Kormendy & Gebhardt 2001; Ferrarese & Ford 2005; Tundo et al. 2006).

Beyond the local universe, M_{BH} can be estimated for active galaxies using the so-called "virial" method. The method assumes that the motion of the broad-line regions (BLR) is dominated by the gravitational potential of the central source. Under this assumption, M_{BH} can be determined from the dynamics of the BLR, provided that velocity and size are measurable, and that some assumption on the orbits is made in order to determine the virial coefficient. The velocity scale of the BLR can be estimated from the width of broad-emission lines, while the size (R_{BLR}) can be measured using "reverberation mapping" (Blandford & McKee 1982), i.e. determining the time lag between continuum changes (presumably originating from an accretion flow) and the corresponding changes in the broad-emission lines. The "virial" assumption has been directly tested for the best studied AGN, NGC 5548. Time lags for NGC 5548 have been determined using several broad lines of different widths, and the inferred distance from the central source shows the expected "virial" correlation for a central point mass, $V \propto R_{BLR}^{-1/2}$ (Peterson & Wandel 2000).

Since the early attempts of determining the time lag between continuum and broad line light curves with cross-correlation methods (e.g. Gaskell & Sparke 1986) and with more sophisticated response function calculations (e.g. Krolik & Done 1995), long-term efforts of reverberation mapping of the local Seyfert galaxies (Wandel et al. 1999) and the low-redshift ($z < 0.2$) PG quasars (Kaspi et al. 2000) have provided clear detections of time lags for about three dozens of highly variable AGNs (Peterson et al. 2004). The measured time lags range from a few to ∼300 days and the nuclear optical luminosities range between 10^{43} and 10^{46} erg s^{-1}. A M_{BH} estimate is then obtained by combining the time-lags with measures of the width of the broad lines and a virial coefficient. The latter can be obtained for example by requiring that AGNs and their host galaxies follow the same M_{BH}-velocity dispersion (σ; or bulge luminosity) relation as quiescent galaxies (Onken et al. 2004; Greene & Ho 2006, Labita et al. 2006). M_{BH} estimates via reverberation mapping are believed to be accurate within a factor of ∼3 (Bentz et al. 2006b; Onken et al. 2004; however, see Krolik 2001).

Reverberation mapping based masses have also provided a widely used empirical method to estimate M_{BH} in distant AGNs from single-epoch data, bypassing the need for observationally expensive time series. This empirically calibrated photo-ionization method (Wandel et al. 1999) is based on the observed correlation between the BLR size (time lag) and optical luminosity at 5100Å.

[1] Department of Physics, University of California, Santa Barbara, CA 93106-9530; woo@physics.ucsb.edu, tt@physics.ucsb.edu
[2] Department of Physics and Astronomy, University of California at Los Angeles, CA 90095-1547, malkan@astro.ucla.edu
[3] Department of Physics, Mail code 103-33, California Institute of Technology, CA 91125.
[4] Lick Observatory, PO Box 85, Mt. Hamilton, CA 95140.

The slope of the power law relation $R_{BLR} \propto L_{5100}^{\alpha}$ with $\alpha \sim 0.5$ is similar to that expected by photoionization models of the BLR (Wandel et al. 1999; Kaspi et al. 2000; Bentz et al. 2006a). This empirical relation has been widely used to determine M_{BH} for large samples of broad-line AGNs, where long-term monitoring efforts would have been prohibitive (e.g. Woo & Urry 2002; McLure et al. 2004). The uncertainty of M_{BH} estimates based on this empirical relation is believed to be a factor of 3-4 (Vestergaard 2002, 2006), and it is due to several factors: i) intrinsic uncertainties in the M_{BH} of local calibrators; ii) intrinsic scatter of the size-luminosity relation; iii) differences between single-epoch measurements of optical luminosity and width, typically available for high-redshift studies, and those obtained from mean or rms spectra obtained from multiple epochs, generally used in the reverberation mapping analysis.

Determining M_{BH} at high redshift is crucial to make progress in a number of outstanding scientific issues, e.g., black hole demographics (Yu & Tremaine 2002), accretion mechanisms (Koratkar & Blaes 1999), connections between galaxy formation and evolution and AGN feedback (Croton 2006; Hopkins et al. 2006), origin of the M_{BH}-σ and other scaling relations (e.g. Silk & Rees 1998; Kauffmann & Haehnelt 2000). Studies of AGN variability at high-redshift and possibly direct reverberation mapping determinations of time lags would be extremely valuable to validate the photoionization method and understand its uncertainty. However, reverberation mapping is challenging for bright quasars at high-redshift because it requires a longer time base line due to the time dilation $(1+z)$ effect. Moreover, high luminosity objects ($L_{5100} \geq 10^{46}$ erg s^{-1}) seem to have smaller amplitudes of continuum variability compared to Seyfert galaxies (variability amplitude-luminosity anticorrelation; Cristiani et al. 1997; Vanden Berk et al. 2004). For example, after six year of monitoring, Kaspi et al. (2006) detected no variability of the Lyα line for 6 high-redshift (z=2.2-3.2) quasars while they detected C IV λ1550 variability (see also Wilhite et al. 2006). These high luminosity quasars show a factor of two smaller continuum variability than that of the lower luminosity PG quasars monitored over a comparable rest-frame period. Lower luminosity type-1 AGNs (Seyfert 1s), although fainter, provide several advantages from the point of view of a monitoring campaign. First and foremost the expected time lags are shorter (order of weeks to a few months), raising the hopes of detecting a lag in only one season, without having to worry about objects observability. Second, variability is expected to be more pronounced since the amplitude of variability seems to be anticorrelated with luminosity.

In this paper we report on our time-domain study of 13 moderate luminosity ($L_{5100} \sim 10^{44}$ erg s^{-1}) AGNs at z $\sim$0.36. The campaign was carried out at the Lick 3-m telescope from May 2004 to November 2004. The sample is drawn from our sample of Seyferts, for which stellar velocity dispersion (Treu, Malkan & Blandford 2004; Woo et al. 2006; hereafter TMB04, W06) and bulge luminosity and radius (Treu et al. 2006 in preparation) have been determined from Keck spectroscopy and Hubble Space Telescope imaging in order to investigate the cosmic evolution of the M_{BH}-σ and M_{BH}-bulge luminosity relations. The goals of this paper are to: i) study the variability of distant seyferts to explore the feasibility of reverberation mapping in the distant universe; ii) study the variability of the Hβ line width to determine the contribution to the systematic uncertainty of the M_{BH} estimated from single epoch spectra as opposed to rms or mean spectra. The paper is organized as follows, In § 2 we describe observations and data reduction. In § 3 we describe continuum and line flux variability. In § 4 we compare line width measurements from single-epoch data. In § 5 we discuss our results and their implications. A standard cosmology is assumed where necessary (H_0=70 kms^{-1}Mpc^{-1}, $\Omega_m = 0.3$ and $\Omega_\Lambda = 0.7$).

2. OBSERVATIONS AND DATA REDUCTION

2.1. *Experiment Design and Sample Selection*

In order to increase our chances to detect a time lag in a single season, we focused our efforts on moderate luminosity AGNs, for which the time lag is predicted to be of order a few weeks in the rest frame, based on the size-luminosity relation (Kaspi et al. 2005). A continuos coverage is critical for a monitoring campaign, but the Lick observatory does not offer service mode observations. Thus, we decided to carry out our campaign over the summer months, when the typical weather patterns at Mt. Hamilton indicate that a relatively large fraction of time is useful for observations (above 80% between June and September[5]). Note that this program does not require photometric conditions, nor particularly good seeing. Of course, the drawback of observing in the summer is the short duration of the nights. Given the expected time lags, we planned observations with weekly cadence (corresponding approximately to 5 days in the rest frame). The Mt. Hamilton and Lick Observatory staff helped enormously by scheduling with regular cadence, except for the obviously longer gaps during full moon periods when the background was prohibitive for optical observations.

The targets are drawn from a parent sample of 30 broad-line AGNs at z=0.365±0.010, initially selected from the Sloan Digital Sky Survey (SDSS) Data Release 2 (Abazajian et al. 2004) to investigate the relation between M_{BH} and their host galaxy properties (for details of sample selection, see W06). A subsample of 13 targets was selected based primarily on observability during the summer months, and secondarily on the availability of ancillary Keck and Hubble data (Table 1).

2.2. *Observations*

All observations were performed with the Shane 3-m telescope at the Lick Observatory between May 10 and November 19. Table 2 shows the journal of observations. The weather was generally bad in May and after the end of September, effectively cutting our campaign to 4 months. A fraction of time was also lost to technical problems. When we could open the dome, observing conditions ranged from photometric to thick cirrus, with a typical seeing $\sim$2". In total, more than 100 individual spectra and images were taken on 20 nights, allowing us to measure variability of continuum and line fluxes.

[5] See http://mthamilton.ucolick.org/techdocs/MH_weather/obstats/prcnt_hrs

We used the Kast double spectrograph with the 600 line mm^{-1} grism centered at $\sim$ 4300Å to obtain blue (3300-5500Å) spectra, and with the 600 line mm^{-1} grating centered at $\sim$ 7500Å to obtain red spectra (6300-9100Å). The pixel scale corresponds to 1.83 Å×0.″8 in the blue and 2.32Å×0.″8 in the red. The blue spectra cover the MgII line (rest wavelength $\sim$ 2798Å) while the red spectra cover the Hβ line (rest wavelength 4861Å) and extend in most cases to the red to include the Hα line. With the 2″ wide slit , the spectral resolution (gaussian dispersion) measured from arc lines was $\sim$ 180 km s^{-1} around the MgII line and $\sim$ 100 km s^{-1} around the Hβ line. Typical exposure time for each object was 2700-3000 second or 2 × 1800 second, yielding S/N $\sim$ 10 per pixel on the continuum of single-epoch spectra.

Internal flat fields for the red spectra were obtained at each target position to correct pixel-to-pixel variation and the fringing pattern of the red CCD. For the blue spectra, internal flats were taken in the afternoon. A set of A0V stars – selected from the Hipparcos catalog to be close in the sky to our targets – was used to correct the A and B-band atmospheric absorption features and to perform secondary flux calibration (see TMB04 and W06 for details). Spectrophotometric standards were observed for flux calibrations.

For spectroscopic target acquisition and to obtain broad band imaging time-series, we used the direct imaging capability of the Kast spectrograph. Before every spectroscopic exposure, we obtained images in the g' and r' bands over the unvignetted field of view of approximately 2 arcminute diameter (0.8 arcsec $pixel^{-1}$). The field of view is large enough that for most objects at least a couple of stars brighter than the target AGN were available for differential photometry. Typical exposure time for imaging was 120 second on the red side with the r' filter and 150 second on the blue side with the g' filter.

2.3. *Data Reduction*

We performed the standard data reduction including flat fielding, wavelength calibration, spectral extraction, and flux calibration using a series of IRAF scripts. Cosmic rays were removed from each exposure using the Laplacian cosmic-ray identification software (van Dokkum 2001). Sky emission lines were used for wavelength calibration in the red, supplemented by arc lamps in the blue. One-dimensional spectra were extracted for maximal S/N with a typical extraction radius of 3 pixels, corresponding to $\sim$ 4.8″. Thirteen low quality spectra with low S/N (mostly due to bad weather) or severe fringing effects (due to imperfect flat-fielding) were removed from the high quality sample to be analyzed for variability. The rest-frame mean and rms spectra for all 13 AGNs are shown in Figure 1, together with the average noise level. Broad MgII, Hβ, Hα and narrow OIII lines are clearly visible in all the average spectra. In most cases, the Hβ line is not visible in the rms spectra since the variation over the observed epochs is smaller than the average uncertainty per pixel. The Hα line is clearly visible in some of the rms spectra.

3. FLUX VARIABILITY

Variability is one of the main characteristics of AGNs, and is the property that is relied upon for reverberation mapping studies. However, the amplitude and the spectral shape change is not well studied for general Seyfert galaxies and quasars. In this section, we first present optical continuum variability (§ 3.1) as determined by broad band g' and r' photometry, using available HST photometry to separate the variable nuclear component from the constant stellar component (§ 3.2). Then, in § 3.3, we study the Hβ line flux variability from the spectroscopic analysis. We focus on the Hβ line since this is the most commonly used line in this redshift range, and the proximity of the narrow OIII lines provides a robust relative spectrophotometric calibration.

3.1. *Continuum flux variability from Lick photometry*

In order to measure continuum variability, we performed differential photometry using stars in the field of each AGN with both g' and r' band images. Three to five stars around the target AGN were typically used to estimate relative flux variations of the AGN. We excluded stars at the edge of the images, where vignetting is problematic. Aperture photometry of individual stars and AGNs was performed using the PHOT task in IRAF, with a 3 pixel (2.4″) aperture radius for flux measurements and with an annulus between 8 and 12 pixels for sky subtraction. The optimal size of the aperture and sky subtraction annulus were determined based on extensive tests with images of various quality seeing. Typical errors in the aperture photometry are 1-3% for the 17-18th magnitude reference stars.

Magnitude differences between AGN and field stars were calculated and then normalized to zero by subtracting the mean difference over all observed epochs. Photometric errors of the target AGN and each star were added in quadrature, yielding total errors on differential photometry in the range 2-4%. Normalized magnitude differences obtained with different stars are consistent within the errors, providing a good sanity check on the analysis. The final light curve and errors were produced by averaging normalized light curves and errors for individual reference stars.

We measured the continuum flux variability for 7 objects, namely S04, S05, S06, S24, S27, S40, and S99, with more than 5 epochs of reliable observations (see Fig. 2, 3 and 4). A continuum broad band light curve for S08 could not be obtained due to the lack of suitable reference stars in the field. The observed flux variability in the g' band, corresponding to rest-frame wavelength 2800-4000Å, is consistent with that of the r' band (rest-frame wavelength 4000-5200Å), but with larger amplitude. In the g' band, peak-to-peak variation is 12-37% and rms variation is 2-10% while in the r' band peak-to-peak variation is 9-32% and rms variation is 2-9% (see Table 3). This amount of variability on week to month timescales is consistent with previous studies of local Seyfert 1 galaxies and quasars (e.g. Webb & Malkan 2000; Klimek et al. 2004) and high-redshift quasars (Kaspi et al. 2003).

3.2. *Continuum nuclear flux and color variability*

Stellar light contributions from host galaxies to the total flux is often significant, especially for Seyfert galaxies (Malkan & Filippenko 1983; Bentz et al. 2006a). This leads to reduced variability in the integrated spectrum and hampers studying color variability of the nucleus (Hawkins 2003).

To investigate nuclear flux and color variability, we need to correct for the host galaxy contamination. This can be achieved using the AGN-galaxy decomposition analysis obtained from HST-ACS F775W (i') band images (GO-10216; PI Treu; Treu et al. 2006, in preparation), and adopting our single-epoch measurement of the nuclear light fraction as our best estimate of the average nuclear light fraction. First, we derived the stellar fraction for the g' and r' bands using:

$$f_m = f_i \times 10^{-0.4[(m-i)_{gal}-(m-i)_{total}]}. \quad (1)$$

Here, f_m is the stellar fraction in each band, f_i is the stellar fraction in the i' band determined from the HST imaging analysis, $(m\text{-}i)_{total}$ is the observed color from the SDSS photometry (DR4), and $(m\text{-}i)_{gal}$ is the stellar light color, $g-r = 1.65 \pm 0.15$ and $r-i = 0.60 \pm 0.06$, as estimated from population synthesis models (Bruzual & Charlot 2003). The uncertainty on the stellar colors represents the spread obtained from models with ages ranging from 1 to 7 Gyr and metallicities from 0.4 to 2.5 solar. Then, we derived intrinsic flux variability by correcting the host galaxy contamination with:

$$R_c = \frac{R-f}{1-f}. \quad (2)$$

Here, f is the stellar fraction in each band, R is the observed variability ($R = F_{total}/ < F_{total} >$), and R_c is the corrected variability ($R_c = F_{AGN}/ < F_{AGN} >$). The mean correction on the variability of 6 objects with HST images is 0.016 magnitude in the g' band and 0.057 magnitude in the r' band. After correcting host galaxy contamination, we find 3-14% rms variation in the g' band and 5-24% in the r' band, somewhat larger in the red for a few objects (see Table 3).

Figure 3 compares the continuum flux variability in the g' and r' bands with and without host galaxy correction. Uncorrected flux variability shows higher amplitude in the g' band than in the r' band ($\Delta g'/\Delta r' = 1.84^{+0.22}_{-0.18}$), as expected because stellar light dilution is more prominent in the red. However the variations become much more similar when the host galaxy contaminations are corrected for ($\Delta g'/\Delta r' = 0.71 \pm 0.06^{+0.13}_{-0.12}$, where errors include a random component and a systematic error from uncertainties in stellar colors). This suggests that the spectral shape in the rest-frame 2800-5200Å does not significantly change on weekly time scales, similar to the findings of Wilhite et al. (2005) that shows an ensemble quasar spectrum is bluer in bright phases only at rest wavelength < 2500Å. The slightly redder colors in bright phases are probably caused by the lack of (or much lower) variability of emission lines, which are included in the wavelength coverage of the brodbands (MgII in blue, and Hβ and [O III] in red), because the relative emission line contribution to the continuum flux is lower in bright phases, producing redder photometric colors (Wilhite et al. 2005).

3.3. *Flux variability of the Hβ line*

Emission line flux variability is more difficult to measure than continuum variability, since the uncertainty in the flux calibration of the ground-based spectroscopy is typically larger than 10%, particularly for faint sources. In the case of AGNs, however, narrow emission lines such as [O III] can be used as internal flux calibrators, since these lines originate from extended low-density regions – probably more than 100 times further from the accretion disk than the BLR (Bennert et al. 2006) – and do not vary on short time scales as broad-emission lines do. Thus, flux variations of broad lines can be measured by normalizing each spectrum to the constant narrow line fluxes, eliminating uncertainties related to slit loss effects, sky transparency, airmass correction, etc. An additional advantage of the specific case of the doublet [O III]$\lambda\lambda$4959,5007 is that the flux ratio between the two components does not vary (Bachall et al. 2004, Dimitrijević et al. 2007) and therefore the rms of the measured ratio provides a robust estimate of the residual uncertainties on the normalized flux.

For 8 objects (S04, S05, S06, S08, S24, S27, S40, S99) with more than 5 reliable single-epoch spectra, we measure Hβ line flux variations using [O III] λ 5007 line as an internal flux calibrator as described below (the procedure is similar to that adopted by local reverberation mapping studies, e.g. Peterson et al. 2002). We also measure the [O III] λ 4959 to [O III] λ 5007 line ratio to help optimize the wavelength windows used for line flux determination[6].

First, we subtract the continuum under Hβ and [O III] lines using the average flux around 4700Å and 5100Å with ~ 50Å windows. We linearly interpolate these two continuum points to define the underlying continuum. Second, we measure the Hβ and [O III] doublet line fluxes by integrating the flux over each line in the optimal windows. Third, the Hβ and [O III] λ 4959 fluxes are normalized by the [O III] λ 5007 flux.

Before we can proceed to determine the intrinsic Hβ line flux variability, we need to account for residual systematic errors in the line ratios ($\sigma_{\rm sys}$). We use the fact that the flux ratio of [O III] λ 5007 and 4959 is constant to obtain a conservative estimate of $\sigma_{\rm sys}$. This is done by requiring that a constant ratio be an acceptable fit to the data as measured by the χ^2 statistic:

$$\sum \frac{[R(i)- < R(i) >]^2}{\sigma(i)^2 + \sigma_{sys}^2} = N-1. \quad (3)$$

Here, R(i) is the flux ratio between [O III] λ4959 and λ5007 at each observed epoch, $\sigma(i)$ is the error in the flux ratio, σ_{sys} is the systematic error, and N is the number of observed epochs. The inferred systematic errors are in the range 2–15%. We note that this is likely to be an upper limit to the systematic errors as λ4959 is weaker than Hβ, and narrow lines fluxes are more sensitive to uncertainties on wavelength calibration and to poor wavelength sampling than broad lines.

Taking random and systematic errors into account, we

[6] The optimal wavelength windows for narrow line flux determination are a tradeoff between the advantages of a small window – high signal-to-noise per pixel, little effects of continuum subtraction uncertainties – and the disadvantages – sensitivity to uncertainties in wavelength calibration as well as to pixelization in the wavelength domain. To find the optimal window we repeated the procedure described below for a range of wavelength regions and picked the one that minimizes the scatter in the [O III] doublet line flux ratio. The choice of the wavelength region for the Hβ line is far less critical since the decline in S/N is more gradual and the spectrograph's pixels are small compared to the line width.

can now estimate the Hβ intrinsic line variability (Table 3). We find rms variability in the range 3–13%. We caution that this should be considered a lower limit due to the fact that our estimate of systematic errors is conservative. For 3 objects we did not detect significant variability.

3.4. *Prospects for reverberation mapping*

We compare flux variations between continuum and the Hβ line flux in Figure 4. The detected Hβ line variability is smaller than the rms variations of the continuum flux (a factor of 2 smaller on average after host galaxy correction), similar to other works (e.g. Rosenblatt & Malkan 1992). Errors on the Hβ flux measurements are larger than those on the continuum flux measurements because the S/N of the spectra is significantly lower than that of broad band images. The light curve of the Hβ flux is qualitatively different from that of continuum flux, possibly indicating a time lag. However, we do not detect a clear lag between continuum and Hβ light curves. This could be due to the fact that the time base line of our campaign is relatively short (4 months at maximum) although the observed variation amplitude (5-10% on Hβ) is comparable to that of the time-lag measured samples in the literature. To illustrate this, in Figure 5 we compared the monitoring time base lines in the rest-frame of each object with the variation amplitude for time-lag detected/undetected samples from the literature. In general a few hundred days of time base lines were required to detect a reliable lag. For high luminosity PG quasars, several years of base lines were used to get a time-lag. Out of 3 objects in our sample (open circles) with the longest time base line ($\sim$100 days in the rest-frame), one object does not show Hβ variability while the other two objects show comparable variability as the Seyfert galaxies with a time lag detection (filled squares). In contrast, rest-frame time base line for our sample is at best in the borderline of the regime, where a reliable time lag can be measured, suggesting that we may detect a time lag if a factor of $\sim$2 longer time base line can be provided.

4. Hβ LINE WIDTH FROM SINGLE-EPOCH DATA

The BLR velocity scale is one of the two ingredients in estimating virial M_{BH}. In reverberation mapping M_{BH} estimates, the FWHM of Balmer lines is generally measured from mean or rms spectra averaged over many observed epochs (Kaspi et al. 2000). In contrast, for most of M_{BH} studies using the size-luminosity relation, relatively low S/N data from a single-epoch observation, e.g. SDSS quasar spectra, are used. This could introduce additional uncertainty to virial M_{BH} estimates, if the width of broad lines varies significantly or the random error on FWHM measurements on single-epoch data is significant. Here, we investigate the uncertainty and variation of the Hβ line width by comparing FWHM from a mean spectrum with that from each spectrum of various observed epochs.

The FWHM of the Hβ line is measured in several steps. First, we subtract continuum under the Hβ line by identifying the continuum levels of each side of the Hβ line and interpolating between them. Second, we subtract [O III] λ4959 by dividing [O III] λ5007 by 3 and blueshifting. Third, we subtract the narrow component of Hβ by rescaling [O III] λ5007 and blueshifting it. Since the FWHM measurements are sensitive to the ratio of narrow Hβ to [O III] (up to $\sim$10%), we used the fixed ratio determined from the high S/N Keck spectra (see Table 3). Fourth, we fit the broad component of Hβ with the Gaussian-Hermite polynomials up to 5-6 orders, depending on the asymmetry of the Hβ line profile, and measure the FWHM of the model (Figure 6). This is necessary because our single-epoch spectra have a typical S/N of 10-15, too low to precisely define wavelengths at the half-maximum.

Figure 7 compares the Hβ FWHM measured from mean spectra with that measured from each single-epoch data for 9 objects with more than 3 reliable spectra. S99 is excluded in this analysis since the Hβ line has such a weak and very broad profile that we could not get meaningful measurements from single-epoch data. With 59 single-epoch data with S/N $\gtrsim$ 10, we find no systematic bias with an average ratio of 1.03 ± 0.02 between single-epoch FWHM and FWHM from mean spectra. The rms scatter around FWHM from mean spectra is $\sim$ 14%, similar to 15-20% scatter found by Vestergaard (2002), who compared one single-epoch FWHM with FWHM from mean spectra for each of 18 AGNs. This scatter is a combination of actual width variation over monthly timescales, and random and systematic errors on single-epoch measurements. For example, Rosenblatt et al. (1992) measured Hβ FWHM using 12 single-epoch spectra for 12 local Seyfert galaxies and found 7-26% rms scatter (mean rms scatter 15%), which were comparable to their FWHM measurement uncertainty.

To understand intrinsic width variation and measurement errors, we measured Hβ FWHM for 8 objects (filled squares), for which high S/N (50-100) Keck single-epoch data are available (W06). The random errors on the FWHM measurements from the Keck spectra are virtually negligible. The rms scatter between the Hβ FWHM from Lick mean spectra and that from Keck single-epoch spectra is 7% (Figure 7). We note that this width variation is much smaller than continuum flux variation as expected from the size-luminosity relation in which log FWHM scales with $1/4 \times \log$ L for given M_{BH}. If we take this scatter as a measure of the intrinsic width variability, then we can consider errors on the Lick single-epoch FWHM to be 12% (0.05 dex), by subtracting 7% (0.03 dex) variation from 14% (0.057 dex) scatter in quadrature. Thus, most of the variation in the single-epoch FWHM measurements seems to be caused by the measurement uncertainty. Consequently, we do not find any correlation between variations in FWHM and continuum or line flux since any intrinsic trend is swamped by measurement errors. If we take 14% scatter as the uncertainty on FWHM measurements, the propagated error in M_{BH} estimates based on single-epoch data is 30%. This estimate should be applied with caution to other single-epoch data sets since the 30% propagated error may not be relevant because of the difference in S/N, the method of FWHM determination, variability, and other factors.

5. DISCUSSION AND CONCLUSIONS

We detected variability of moderate luminosity ($L_{5100} \sim 10^{44}$ erg s^{-1}) AGNs at z=0.36. Continuum flux variability in the rest-frame wavelength 2800-4000Å and 4000-5200Å is detected at the 2-10% level (rms vari-

ation). These measurements are consistent with other variability studies of local Seyfert galaxies and higher redshift quasars (e.g. Webb & Malkan 2000; Kaspi et al. 2000). After correcting for stellar light contamination using HST-ACS images, we find that the intrinsic nuclear continuum variability is 3-25%. Blue and red continuum variability correlates, indicating that the spectral shape does not significantly change on weekly time scales.

We also detected intrinsic Hβ line flux variability at the level of 3-13%, on average a factor of 2 lower than the continuum flux variability. Light curves of the continuum flux and the Hβ line flux are qualitatively different, perhaps due to a time lag. However, the time base line of our campaign seems to be too short to detect a reliable lag. We may detect a time lag if a longer time base line can be provided. With modern scheduling techniques and perhaps a robotic telescope, light curves could be extended to 8 months per year.

Finally we study variability of the Hβ line width to estimate uncertainties in M_{BH} estimates from single-epoch data. We compare the Hβ FWHM measured from high S/N mean spectrum with that measured from each single-epoch spectrum. We find 14% scatter around the one-to-one relationship, most of which comes from random errors on FWHM measurements using single-epoch spectra. M_{BH} estimated from single-epoch spectra with typical S/N of 10-15 has 30% uncertainty due to the line width measurement errors. This uncertainty is significantly smaller than the total uncertainty of M_{BH} estimates from single-epoch data (a factor of 3-4; Vestergaard 2002), indicating uncertainties on FWHM may not be a dominant source of uncertainties on virial M_{BH}, estimates.

We thank the anonymous referee for a careful reading of the manuscript and numerous suggestions that improved the presentation of our results. We thank Aaron Barth, Roger Blandford, Omer Blaes and Brad Peterson for numerous stimulating conversations. This work is based on data collected at the Lick Observatory – operated by the University of California – and with the Hubble Space Telescope operated by AURA under contract from NASA. We are grateful to the Shane 3-m staff for their help during the observations and Graeme Smith for help with the scheduling. We thank Alex Filippenko and Ryan Foley for obtaining some of the data for us. This project is made possible by the wonderful public archive of the Sloan Digital Sky Survey. We acknowledge financial support by NASA through HST grant GO-10216.

REFERENCES

Abazajian, K., et al. 2004, AJ, 128, 502
Bahcall, J. N., Steinhardt, C. L., & Schlegel, D. 2004, ApJ, 600, 520
Bentz, M. C., Peterson, B. M., Pogge, R. W., Vestergaard, M., & Onken, C. A. 2006a, ApJ, 644, 133
Bentz, M. C., et al. 2006b, ApJ, 651, 775
Blandford, R. D., & McKee, C. F. 1982, ApJ, 255, 419
Bruzual, G., & Charlot, S. 2003, MNRAS, 344, 1000
Cristiani, S., Trentini, S., La Franca, F., & Andreani, P. 1997, A&A, 321, 123
Dietrich, M., et al. 1994, A&A, 284, 33
Dimitrijević, M. S., Popović, L. Č., Kovačević, J., Dačić, M., & Ilić, D. 2007, MNRAS, 374, 1181
Erkens, U., et al. 1995, A&A, 296, 90
Ferrarese, L., & Merritt, D. 2000, ApJ, 539, L9
Ferrarese, L., & Ford, H. 2005, Space Science Reviews, 116, 523
Gaskell, C. M., & Sparke, L. S. 1986, ApJ, 305, 175
Gebhardt, K., et al. 2000, ApJ, 539, L13
Greene, J. E., & Ho, L. C. 2006, ApJ, 641, L21
Häring, N., & Rix, H.-W. 2004, ApJ, 604, L89
Hawkins, M. R. S. 2003, MNRAS, 344, 492
Jackson, M., et al. 1992, A&A, 262, 17
Kaspi, S., Smith, P. S., Netzer, H., Maoz, D., Jannuzi, B. T., & Giveon, U. 2000, ApJ, 533, 631
Kaspi, S., Netzer, H., Maoz, D., Shemmer, O., Brandt, W. N., & Schneider, D. P. 2003, ASP Conf. Ser. 290: Active Galactic Nuclei: From Central Engine to Host Galaxy, 290, 615
Kaspi, S., Maoz, D., Netzer, H., Peterson, B. M., Vestergaard, M., & Jannuzi, B. T. 2005, ApJ, 629, 61
Kaspi, S., Brandt, W. N., Maoz, D., Netzer, H., Schneider, D. P., & Shemmer, O. 2006, ArXiv Astrophysics e-prints, arXiv:astro-ph/0612722
Kauffmann, G., & Haehnelt, M. 2000, MNRAS, 311, 576
Klimek, E. S., Gaskell, C. M., & Hedrick, C. H. 2004, ApJ, 609, 69
Koratkar, A., & Blaes, O. 1999, PASP, 111, 1
Kormendy, J., & Gebhardt, K. 2001, AIP confrence proceedings, 586, 363
Krolik, J. H. 2001, ApJ, 551, 72
Krolik, J. H., & Done, C. 1995, ApJ, 440, 166
Labita, M., Treves, A., Falomo, R., & Uslenghi, M. 2006, MNRAS, 373, 551
Magorrian, J., et al. 1998, AJ, 115, 2285
Malkan, M. A., & Filippenko, A. V. 1983, ApJ, 275, 477
Marconi, A., & Hunt, L. K. 2003, ApJ, 589, L21
McLure, R. J., & Dunlop, J. S. 2004, MNRAS, 352, 1390
Onken, C. A., Ferrarese, L., Merritt, D., Peterson, B. M., Pogge, R. W., Vestergaard, M., & Wandel, A. 2004, ApJ, 615, 645
Peterson, B. M., & Wandel, A. 2000, ApJ, 540, L13
Peterson, B. M., et al. 2002, ApJ, 581, 197
Peterson, B. M., et al. 2004, ApJ, 613, 682
Rosenblatt, E. I., Malkan, M. A., Sargent, W. L. W., & Readhead, A. C. S. 1992, ApJS, 81, 59
Rosenblatt, E. I., Malkan, M. A., Sargent, W. L. W., & Readhead, A. C. S. 1994, ApJS, 93, 73
Silk, J., & Rees, M. J. 1998, A&A, 331, L1
Stirpe, G. M., et al. 1994, A&A, 285, 8574
Tundo, E., Bernardi, M., Hyde, J. B., Sheth, R. K., & Pizzella, A. 2006, ArXiv Astrophysics e-prints, arXiv:astro-ph/0609297
Vanden Berk, D. E., et al. 2004, ApJ, 601, 692
van der Marel, R. P., & Franx, M. 1993, ApJ, 407, 525
van Dokkum, P. G. 2001, PASP, 113, 1420
Vestergaard, M. 2002, ApJ, 571, 733
Vestergaard, M., & Peterson, B. M. 2006, ApJ, 641, 689
Wandel, A., Peterson, B. M., & Malkan, M. A. 1999, ApJ, 526, 579
Webb, & Malkan, A. 2000, ApJ, 540, 652
Wilhite, B. C., Vanden Berk, D. E., Kron, R. G., Schneider, D. P., Pereyra, N., Brunner, R. J., Richards, G. T., & Brinkmann, J. V. 2005, ApJ, 633, 638
Treu, T., Malkan, M., & Blandford, R. D. 2004, ApJ, 615, L97 (TMB04)
Woo, J.-H., & Urry, C. M. 2002, ApJ, 579, 530
Woo, J.-H., Treu, T., Malkan, M. A., & Blandford, R. D. 2006, ApJ, 645, 900 (W06)
Yu, Q., & Tremaine, S. 2002, MNRAS, 335, 965

TABLE 1
Targets

(1) Name	(2) z	(3) RA (J2000)	(4) DEC (J2000)	(5) r'
S04 (J210211.50-064645.0)	0.3580	21 02 11.51	-06 46 45.03	18.75
S05 (J210451.83-071209.4)	0.3531	21 04 51.85	-07 12 09.45	18.43
S06 (J212034.18-064122.2)	0.3689	21 20 34.19	-06 41 22.24	18.53
S08 (J235953.44-093655.6)	0.3591	23 59 53.44	-09 36 55.53	18.61
S09 (J005916.10+153816.0)	0.3548	00 59 16.11	+15 38 16.08	18.33
S12 (J021340.59+134756.0)	0.3575	02 13 40.60	+13 47 56.06	18.18
S23 (J140016.65-010822.1)	0.3515	14 00 16.66	-01 08 22.19	18.22
S24 (J140034.70+004733.3)	0.3621	14 00 34.71	+00 47 33.48	18.43
S26 (J152922.24+592854.5)	0.3691	15 29 22.26	+59 28 54.56	18.93
S27 (J153651.28+541442.6)	0.3667	15 36 51.28	+54 14 42.71	18.87
S28 (J161156.29+451611.0)	0.3682	16 11 56.30	+45 16 11.04	18.78
S40 (J012655.82+153357.8)	0.3749	1 26 55.82	+15 33 57.87	18.62
S99 (MS 1558.3+4138)	0.3690	16 00 02.80	+41 30 27.00	18.78

Note. — Col. (1): Target ID. Col. (2): Redshift. Col. (3): RA. Col. (4): DEC. Col. (5): Extinction corrected r' AB magnitude from SDSS photometry.

TABLE 2
Journal of observations

Run	Date	Targets	Seeing arcsec	Conditions
(1)	(2)	(3)	(4)	(5)
1	2004 May 10	S26,S99	2.4-3	clear/fog,humidity
2	2004 May 18	S05,S23,S24,S27,S99	1.7-1.8	clear
3	2004 May 25	S23,S24,S26,S27,S28,S99	2.0-2.2	photometric
4	2004 Jun 1	S05,S24,S26,S27,S28,S99	1.8-2.2	photometric
5	2004 Jun 11	S05,S24,S26,S27,S28,S99	1.8-2.4	cirrus
6	2004 Jun 20	S05,S24,S26,S27,S28,S99	2.1-2.8	cirrus
7	2004 Jun 29	S05,S24,S26,S27,S28,S99	2.2-2.9	clear
8	2004 Jul 9	S24,S27,S99	1.5-1.6	clear/instrument failure
9	2004 Jul 14	S05,S24,S27,S28,S99	2.2-2.4	clear
10	2004 Jul 18	S04,S05,S06,S27	2-3	cirrus
11	2004 Aug 6	S04,S05,S06,S08,S09,S27,S99	1.7-2.	photometric/CCD problem
12	2004 Aug 14	S04,S05,S06,S08,S09,S27,S99	2.2-3	clear/cirrus
13	2004 Aug 24	S04,S05,S06,S08,S09,S27,S99	1.7-2	cirrus
14	2004 Sep 8	S04,S05,S06,S08,S09,S12,S27,S40,S99	1.3-1.7	clear/guider problem
15	2004 Sep 15	S04,S05,S06,S08,S09,S12,S27,S40,S99	1.4-1.8	photometric
16	2004 Sep 22	S04,S05,S08,S09,S12,S27,S40,S99	1.3-2.4	cirrus
17	2004 Sep 30	S04,S05,S06,S08,S09,S27,S40	1.4-1.8	cirrus
18	2004 Oct 11	S04,S05,S06,S08,S09,S12,S27,S40	1.8-2.2	photometric/instrument problem
19	2004 Oct 20	S09,S40	2-3	cloud,humidity
20	2004 Nov 3			rain
21	2004 Nov 19	S12,S40	2.5-2.7	clear

Note. — Col. (1): Observing run. Col. (2): Observing date. Col. (3): targets. Col. (4): Seeing (FWHM) measured from r' band direct imaging. Col. (5): Conditions/Notes.

TABLE 3
VARIABILITY

Target (1)	# of epochs (2)	$max_{g'}$ (3)	$rms_{g'}$ (4)	$e_{g'}$ (5)	$rms_{g'c}$ (6)	$max_{r'}$ (7)	$rms_{r'}$ (8)	$e_{r'}$ (9)	$rms_{r'c}$ (10)	rms([O III]) (11)	$\sigma_{sys.}$ (12)	rms(Hβ) (13)	Hβ/[O III] (14)
S04	8/8/9	0.338	0.098	0.026	0.118	0.096	0.022	0.024	0.058	0.102	0.068	0.060	0.07
S05	14/13/10	0.121	0.026	0.026	0.029	0.111	0.028	0.024	0.049	0.084	0.051	0.081	0.10
S06	9/8 /5	0.217	0.061	0.064	0.079	0.208	0.042	0.043	0.127	0.014	-	-	0.10
S08	0/0/8	-	-	-	-	-	-	-	-	0.200	0.162	-	0.10
S24	6/7/6	0.245	0.078	0.044	0.098	0.300	0.099	0.037	0.243	0.111	0.053	0.049	0.08
S27	16/17/15	0.289	0.078	0.045	0.090	0.210	0.034	0.033	0.075	0.165	0.107	-	0.18
S40[1]	5/5/5	0.147	0.032	0.057	-	0.100	-	0.054	-	0.035	0.016	0.029	0.07
S99	14/15/11	0.338	0.072	0.050	0.136	0.197	0.040	0.028	0.193	0.066	0.020	0.130	0.10

REFERENCES. — 1) no HST image available.

NOTE. — Col. (1): Target ID. Col. (2): Number of flux points in the g' and r' band images and Hβ line flux. Col. (3): peak to peak variation in magnitude in g' Col. (4): rms variation in g' Col. (5): mean error in g' Col. (6): rms variation in g' after stellar contribution correction. Col. (7): peak to peak variation in magnitude in r' Col. (8): rms variation in r' Col. (9): mean error in r' Col. (10): rms variation in r' after stellar contribution correction. Col. (11): rms scatter of the [O III] λ5007 to [O III] λ4959 flux ratio. Col. (12): Systematic errors on Hβ estimated as described in Section 3.3 Col. (13) Intrinsic rms Hβ flux variation in magnitudes after correcting systematic errors. Col. (14) narrow Hβ component to [O III] λ5007 flux ratio, used to remove narrow Hβ component before measuring broad Hβ FWHM.

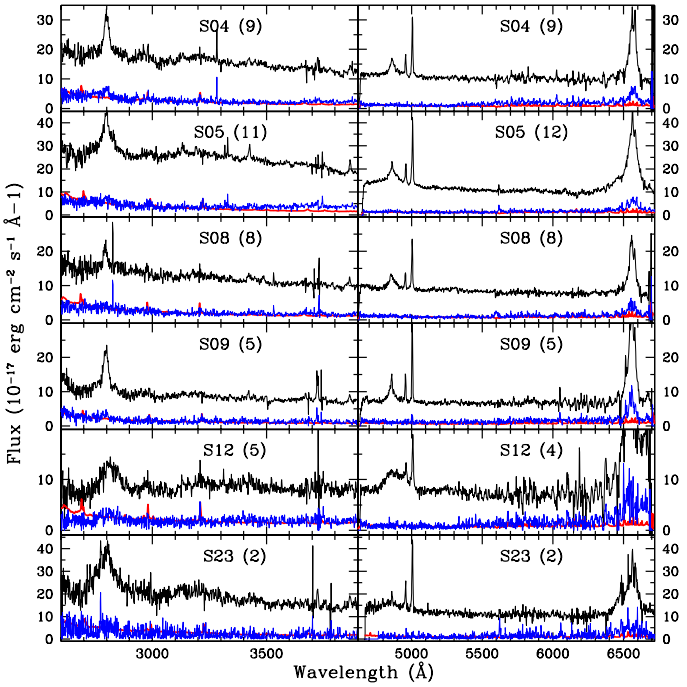

FIG. 1.— Mean (black) and rms (blue) spectra of all observed AGNs, covering MgII, Hβ, and Hα lines, with the average noise level (red). The number of combined spectra is designated for each objects. For S06 and S99, blue spectra are excluded since MgII line is not well defined due to the much lower S/N ratios.

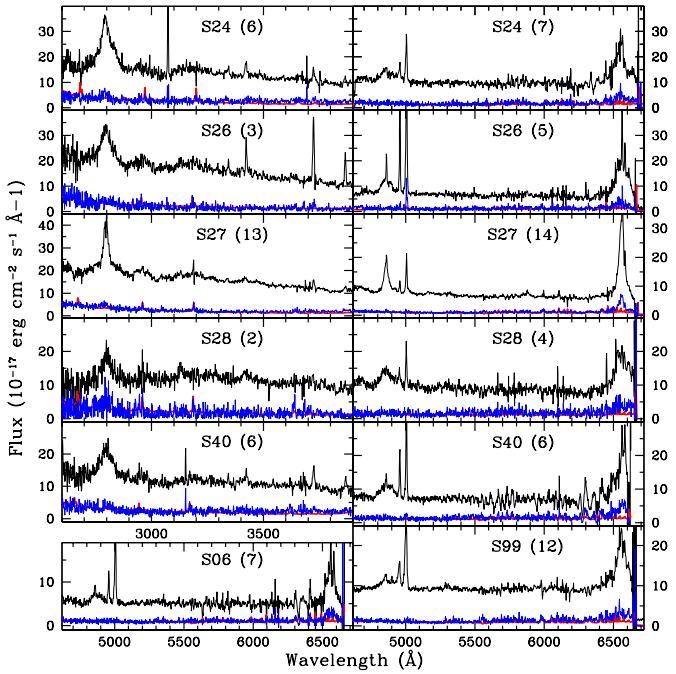

Fig. 1. — Continued

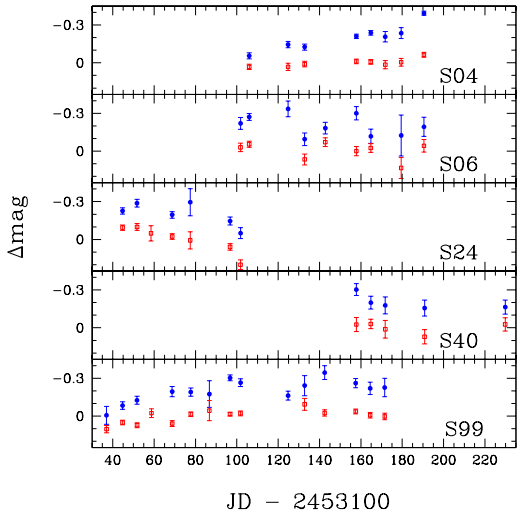

FIG. 2.— Examples of light curves in the g' and r' bands. Differential photometry was obtained by comparison with nearby stars in the imaging field as described in Section 3.1. For clarity, g' band light curves (blue circles) are offset by 0.2 magnitudes.

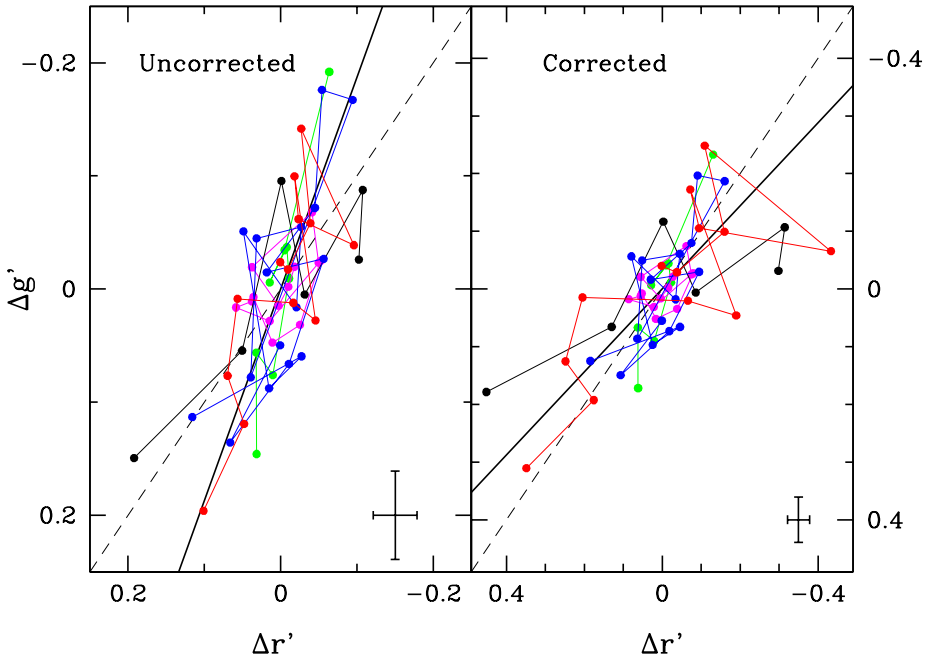

FIG. 3.— Comparison of variability in g' and r' bands. Left: observed flux variability. Individual AGNs are denoted with different colors (green: S04, magenta: S05, yellow: S06, black: S24, blue: S27, red: S99). Note that variations in g' and r' band are correlated, with a larger amplitude in the blue band. The solid line is the best fit slope, $1.84^{+0.22}_{-0.18}$, significantly larger than unity (dashed line), suggesting that spectra look bluer when brighter. Right: Nuclear flux variability after correcting for the stellar contribution using HST-ACS images. Note that the amplitude of the nuclear variations is larger and the plotting range is larger than in the left panel. The best fit slope is now $0.71 \pm 0.06^{+0.13}_{-0.12}$, where errors include a random component and a systematic error from uncertainties in stellar colors. This is marginally consistent with unity, suggesting approximately achromatic intrinsic luminosity variations over this wavelength range 2800-5200Å. Typical errors are plotted at the bottom-right of each panel.

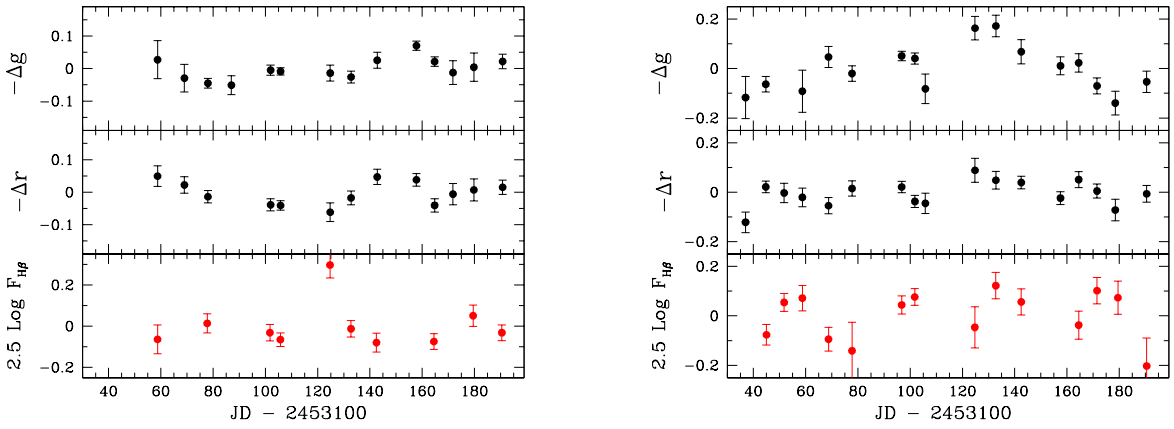

FIG. 4.— Light curves of the continuum flux and the Hβ line flux for S05 and S27. For each object the continuum flux variability is shown in the g' band (top) and the r' band (middle). The Hβ line flux light curve is shown in the bottom panel. Note that the amplitude of the variations is similar to that of the broad band.

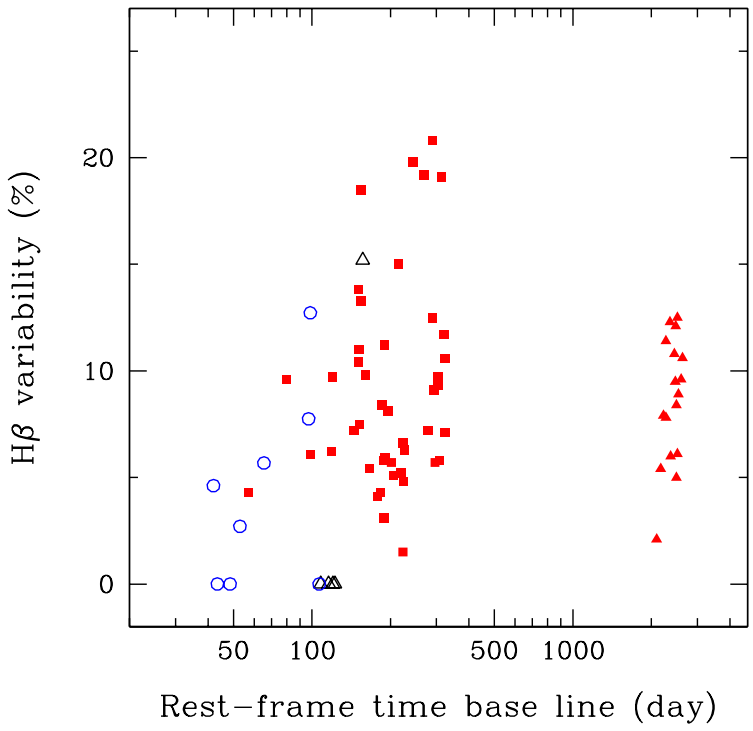

FIG. 5.— Hβ variability vs. rest-frame time base line for various samples. Time lag detected Seyferts (filled squares) and PG quasars (filled triangles) are from the compilation of Peterson et al. (2004). AGNs with no or unreliable time lag detection are denoted with open symbols (circles: our Seyferts at z=0.4; triangles: 5 AGNs from Lovers of AGNs campaign, Jackson et al. 1992; Dietrich et al. 1994; Stirpe et al. 1994; Erkens et al. 1995). Time base line for time lag measured sample is generally more than a few hundreds days in the rest-frame. In contrast, time base line for our sample is relatively short (<100 days) although variability of the Hβ line flux is comparable to that of the time-lag measured Seyferts.

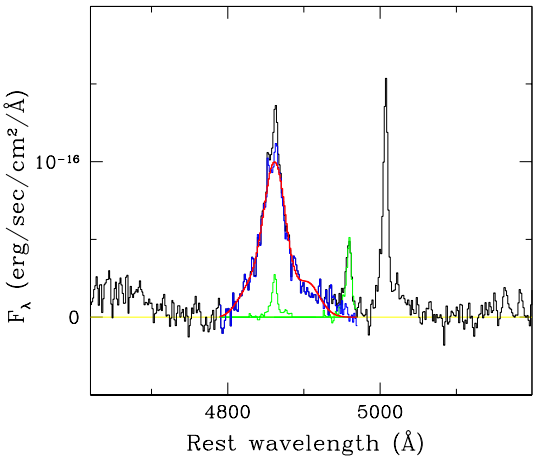

FIG. 6.— Example of the Hβ FWHM measurement using Gaussian-Hermite polynomials. After removing the narrow Hβ and [O III] λ4959 with a rescaled and blueshifted [O III λ5007 line profile (green), Gaussian-Hermitian models (red) are used to fit the broad Hβ line (blue). The FWHM of the line is then measured on the model fit.

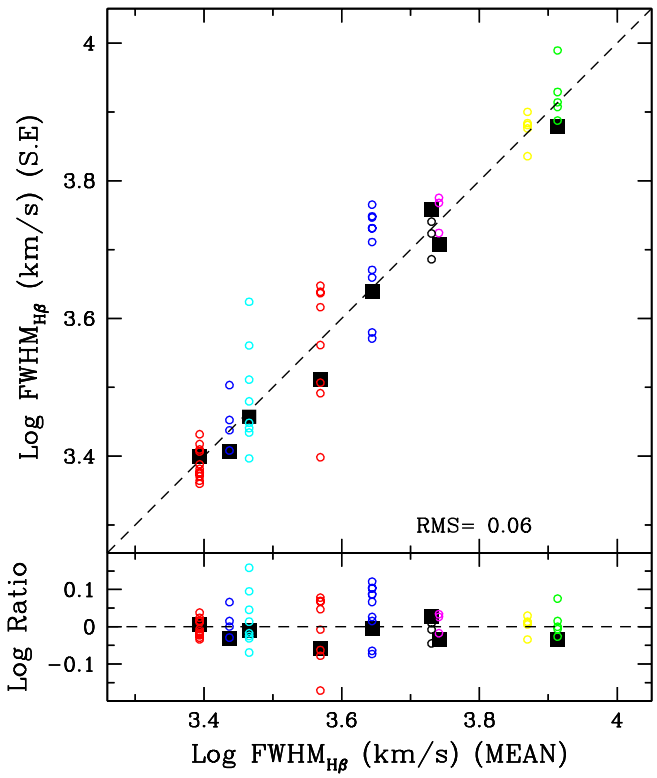

FIG. 7.— Comparison of the Hβ FWHM measured from mean spectra with those measured from various single-epoch spectra. Single-epoch FWHMs are consistent with FWHM from mean spectra with an average ratio of 1.03 ± 0.02. The rms scatter around FWHM from mean spectra is 14%, indicating uncertainties of M_{BH} estimates based on single-epoch data can be 30% due to the random errors in measuring FWHM. For comparison, we show FWHM measurements using high S/N Keck data (filled squares), which are consistent with FWHM of mean spectra with a rms scatter $\sim$0.03 dex, indicating intrinsic FWHM variation is $\sim$7%.